Thermal and Light-Induced Spin Crossover Phenomena in New 3D Hofmann-Like Microporous Metalorganic Frameworks Produced As Bulk Materials and Nanopatterned Thin Films

Gloria Agustí,[†] Saioa Cobo,[‡] Ana B. Gaspar,[†] Gábor Molnár,[‡] Nawel Ould Moussa,[‡] Petra Á. Szilágyi,[‡,§] Villö Pálfi,[‡,§] Christophe Vieu,[||] M. Carmen Muñoz,[⊥] José Antonio Real,*[,†] and Azzedine Bousseksou*[,‡]

Instituto de Ciencia Molecular/Departamento de Química Inorgánica, Universidad de Valencia, Edificio de Institutos de Paterna, Apartado de correos 22085, 46071 Valencia, Spain, Laboratoire de Chimie de Coordination, CNRS UPR8241, 205, Route de Narbonne, 31077 Toulouse, France, Institute of Chemistry, Eötvös Loránd University, Pázmány P. sétány 1/A, H-1117 Budapest, Hungary, Laboratoire d'Analyse et d'Architecture des Systèmes, CNRS UPR8001, 7 avenue du Colonel Roche, 31077 Toulouse, France, and Departamento de Física Aplicada, Universidad Politécnica de Valencia, Camino de Vera s/n, 46022, Valencia, Spain

Received July 23, 2008. Revised Manuscript Received September 11, 2008

Three novel three-dimensional coordination polymers, $\{Fe^{II}(azpy)[(M^{II}(CN)_4)]\}\cdot nH_2O$ (azpy = 4,4′-azopyridine; M = Ni, Pd, and Pt), have been synthesized as polycrystalline bulk materials and as continuous as well as nanopatterned thin films on gold substrates. Single crystals of the Pt derivative have also been isolated and the corresponding X-ray diffraction analysis at 140 K indicates that it crystallizes in the tetragonal *P*4/*mmm* space group with $a = b = 7.1670(5)$ Å, $c = 13.0330(13)$ Å, $V = 669.40(9)$ Å^3 and $Z = 1$. Four square-planar $[Pt(CN)_4]^{2-}$ anions occupy the equatorial positions of $[Fe^{II}N_6]$ octahedron and four Fe(II) atoms are coordinated to each $[Pt(CN)_4]^{2-}$ anion, thereby defining an infinite set of 2D planar layers pillared by the azpy ligands which bridge through the axial positions consecutive Fe(II) atoms. Magnetic susceptibility, calorimetric, and Mössbauer measurements reveal the occurrence of a thermal spin crossover phenomenon in the powder samples, which depends strongly on the water-content of the lattice in the case of Pd and Pt derivatives. The spin crossover is less cooperative with $T_c = 245$ K in the case of Ni, but the Pd (Pt) analogues display almost complete spin transitions with a hysteresis loop centered around 292 (280) and 191 (183) K, in the hydrated and dehydrated forms, respectively. Thin films of the three compounds were grown via a sequential assembly method using coordination reactions. Raman spectroscopic study proves that thermal spin crossover, similar to the bulk forms, occurs in the films. With the exception of the bulk Ni complex, a virtually complete light-induced spin conversion (LIESST effect) is detected by Raman spectroscopy in the thin films as well as in the powders below ca. 130 K.

Introduction

Iron(II) spin crossover (SCO) complexes are of current interest in chemistry and materials science, not only because of their intrinsic fundamental properties[1] but also because of their potential applications as functional materials for the construction of sensor and memory devices.[2] They can be reversibly switched between two electronic configurations, low-spin (LS) and high-spin (HS), by an external action like change of temperature, pressure, light irradiation, pulsed magnetic fields, and even by chemical species (e.g., guest molecules). The two states reveal differences in magnetism, optical properties, dielectric constant, and crystal structure. Furthermore, strong elastic interactions between the metal ions may give rise to a first-order phase transition with hysteresis (memory effect) between the HS and LS forms. During the last two decades, several synthetic strategies have been proposed to obtain such interesting properties. These strategies typically have required the use of bis-monodentate pyridine-, triazole-, or tetrazole-derived ligands. More recently, the use of cyanometalate anions as bridging ligands has given a great impulse to this field through the investigation of new Hofmann-like polymeric SCO compounds.[1d,e,g]

* Corresponding author. Fax: 34-963544359 (J.R.); 33-(0)561553003 (A.B.). E-mail: Jose.A.Real@uv.es (J.R.); boussek@lcc-toulouse.fr (A.B.).
[†] Universidad de Valencia.
[‡] CNRS UPR8241.
[§] Eötvös Loránd University.
[||] CNRS UPR8001.
[⊥] Universidad Politécnica de Valéncia.

(1) (a) *Spin Crossover in Transition Metal Compounds I−III*; Gütlich, P., Goodwin, H. A., Eds.; Topics in Current Chemistry; Springer: New York, 2004; Vol 233−235. (b) Gütlich, P.; Hauser, A.; Spiering, H. *Angew. Chem., Int. Ed.* **1994**, *33*, 2024. (c) Bousseksou, A.; Molnár, G.; Matouzenko, G. *Eur. J. Inorg. Chem.* **2004**, 4353. (d) Real, J. A.; Gaspar, A. B.; Muñoz, M. C. *Dalton Trans.* **2005**, 2062. (e) Real, J. A.; Gaspar, A. B.; Niel, V.; Muñoz, M. C. *Coord. Chem. Rev.* **2003**, *236*, 121. (f) Gaspar, A. B.; Ksenofontov, V.; Seredyuk, M.; Gütlich., P. *Coord. Chem. Rev.* **2005**, *249*, 2661. (g) Garcia, Y.; Niel, V.; Muñoz, M. C.; Real, J. A. *Top. Curr. Chem.* **2004**, *233*, 229.

(2) (a) Kahn, O.; Kröber, J.; Jay, C. O. *Adv. Mater.* **1992**, *4*, 718. (b) Kahn, O.; Martinez, C. J. *Science* **1998**, *279*, 44. (c) Létard, J.-F.; Guionneau, P.; Goux-Capes, L. *Top. Curr. Chem.* **2004**, *235*, 221. (d) Bousseksou, A.; Molnár, G.; Demont, P.; Menegotto, J. *J. Mater. Chem.* **2003**, *13*, 2069. (e) Galet, A.; Gaspar, A. B.; Muñoz, M. C.; Bukin, G. V.; Levchenko, G.; Real, J. A. *Adv. Mater.* **2005**, *17*, 2949.

10.1021/cm8019878 CCC: $40.75
Published on Web 10/11/2008

One of the most prominent examples is represented by the family of compounds $\{Fe^{II}(pyrazine)[M^{II}(CN)_4]\}$ (M = Ni, Pd, or Pt).[3] In these isostructural three-dimensional (3D) coordination networks a number of important singularities come together: (i) they undergo cooperative spin transitions at high temperatures accompanied by large hysteresis loops; (ii) drastic color and structural changes are also observed around room temperature; (iii) porosity is an additional singularity of these 3D networks in which host−guest interactions have considerable effects on the SCO properties of these materials.[4,5] These facts, together with the observation of photoswitching between the high spin (HS) and low spin (LS) states within the hysteresis loop using a pulsed laser at room temperature,[6] make this kind of materials highly valuable.

Obviously, in a first step, this research requires the study of bulk samples. However, for sensor and memory applications as well as for optical studies the materials require, in general, to be processed as thin films or nanoparticles. Up to now, only a small number of spin crossover compounds have been processed in such a way, i.e., Lagmuir−Blodgett films,[7] liquid crystal films,[8] embedded in nafion films[9] or nanoparticles of the 1,2,4-triazole iron(II) family.[10] In this line, we have recently reported the first successful assembly of multilayer films on gold surfaces as well as the synthesis of nanocrystals of the coordination polymer $\{Fe(pyrazine)[Pt^{II}(CN)_4]\}$. These films and nanocrystals display thermal spin crossover phenomenon with hysteresis around room temperature.[11,12] In addition to this property, the possibility to fabricate nanometric patterns of these films by lift-off[13] and synthesize ultrasmall nanoparticules by solution chemistry[14] has been shown recently.

As a new step in this research, here we report a new family of SCO Hofmann-like coordination polymers based on bridging $[M(CN)_4]^{2-}$ counterions and organic ligands other than pyrazine. In particular, we present the synthesis, crystal structure and physical characterization of microcrystalline bulk samples and thin films of $\{Fe(azpy)[M(CN)_4]\}\cdot nH_2O$ [$n \leq 1$; azpy = 4,4′-azopyridine; M = Ni (**1a**, **1b**), Pd (**2a**, **2b**), and Pt (**3a**, **3b**), where **a** stands for the hydrated and **b** the dehydrated form].

Experimental Section

Materials. $Fe(BF_4)_2\cdot 6H_2O$, $K_2Ni(CN)_4$, $K_2Pd(CN)_4$, $K_2Pt(CN)_4$, and tetrabutylammonium bromide (TBABr) were purchased from commercial sources and used as received. The ligand azpy was prepared by oxidative coupling of 4-aminopyridine by hypochlorite. A cold solution of 50 mL of 4-aminopyridine (26 mmol) in water was added dropwise to 300 mL of a 5% NaOCl (0.201 mol) solution. The mixture was stirred at 0 °C. The orange precipitate was then filtered and washed with cool water. Recrystallization in water yielded 4,4′-azopyridine as long orange needles (yield: 60%). $\{(TBA)_2[M^{II}(CN)_4)]\}$ (M = Ni, Pd or Pt) salts were synthesized by mixing slowly an aqueous solution of $K_2M(CN)_4$ (M = Ni, Pt or Pd) (0.53 mmol) with a solution of TBABr (1.06 mmol). After several days colorless crystals of the complex were formed. Crystals were washed to dissolve the rest of KBr, and dried in air at room temperature.

Synthesis of $\{Fe(azpy)[M(CN)_4]\}\cdot nH_2O$ (M = Ni, Pd, or Pt) (1a−3a). The synthesis was performed under nitrogen atmosphere. To a methanolic solution containing $Fe(BF_4)_2\cdot 6H_2O$ (100 mmol, 25 mL) was added dropwise a solution of azpy in MeOH (1 mmol, 25 mL). To the resulting orange solution was added 1 mmol of the $K_2M(CN)_4$ salts (M = Ni, Pd or Pt) dissolved in 25 mL of water leading to the formation of a dark green precipitate (Ni) or dark violet precipitates (Pd, Pt). The precipitates were filtered off and washed with MeOH and H_2O and subsequently dried under a N_2 flow. Yield: 60% (**1a**), 70% (**2a**), 70% (**3a**). Anal. Calcd for **1a**, $C_{14}H_{10}N_8OFeNi$: C, 39.96; H, 2.40; N, 26.63. Found: C, 39.49; H, 2.32; N, 26.57. EDAX (energy-dispersive X-ray analysis) for **1a**: Fe, 48.7; Ni, 51.3. Anal. Calc. for **2a**, $C_{14}H_{10}N_8OFePd$: C, 35.89; H, 2.15; N, 23.92. Found: C, 35.44; H, 2.07; N, 23.84. EDAX for **2a**: Fe, 48.7; Pd, 51.3. Anal. Calcd for **3a**, $C_{14}H_{10}N_8OFePt$: C, 30.18; H, 1.81; N, 20.11. Found: C, 30.04; H, 1.77; N, 20.09. EDAX for **3a**: Fe, 52.6; Pt, 47.4.

Single crystals of **3a** where grown using a slow diffusion technique. One side of an H-shaped vessel contains a mixture of $(NH_4)_2Fe(SO_4)_2\cdot 6H_2O$ (0.127 mmol, 50 mg) in water (0.5 mL). The other side contains a methanol−water solution (1:1) (1 mL) of azpy (0.127 mmol, 23 mg) and $K_2Pt(CN)_4$ (0.127 mmol, 48 mg). Square-shaped orange crystals of **3a** suitable for single-crystal X-ray analysis were obtained after 3 weeks. Agglomerations of single crystals originate the same violet color as the microcrystalline powder.

Synthesis of $\{Fe(azpy)[M(CN)_4]\}$ (M = Ni, Pd, or Pt) (1b−3b). The dehydrated compounds have been obtained by heating at 160 °C during 30 min the compounds **1a**−**3a** as shown by thermogravimetric analysis performed using a Mettler-Toledo SDTA851 system (see the Supporting Information). Anal. Calcd for **1b**: $C_{14}H_8N_8FeNi$: C, 41.74; H, 2.00; N, 27.82. Found: C, 41.49; H, 1.99; N, 27.57. EDAX for **1b**: Fe, 48.7; Ni, 51.3. Anal. Calcd for **2b**: $C_{14}H_8N_8FePd$: C, 37.32; H, 1.79; N, 24.87. Found: C, 37.14; H, 1.69; N, 24.84. EDAX for **2b**: Fe, 48.7; Pd, 51.3. Anal. Calcd for **3b**: $C_{14}H_8N_8FePt$: C, 31.19; H, 1.50; N, 20.78. Found: C, 31.04; H, 1.47; N, 20.69. EDAX for **3b**: Fe, 52.6; Pt, 47.4.

Synthesis of 1b−3b as Thin Films. Thin films were assembled on gold surfaces (15 nm Au/2 nm Ti evaporated on polished Si(100)

(3) Niel, V.; Martínez-Agudo, J. M.; Muñoz, M. C.; Gaspar, A. B.; Real, J. A. *Inorg. Chem.* **2001**, *40*, 3838.
(4) Niel, V. PhD thesis, University of Valencia, Valencia, Spain, 2002.
(5) Galet, A. PhD thesis, University of Valencia, Valencia, Spain, 2007.
(6) (a) Bonhommeau, S.; Molnár, G.; Galet, A.; Zwick, A.; Real, J. A.; McGarvey, J. J.; Bousseksou, A. *Angew. Chem., Int. Ed.* **2005**, *44*, 4069. (b) Cobo, S.; Ostrovskii, D.; Bonhommeau, S.; Vendier, L.; Molnár, G.; Salmon, L.; Tanaka, K.; Bousseksou, A. *J. Am. Chem. Soc.* **2008**, *130*, 9019.
(7) (a) Soyer, H.; Mingotaud, C.; Boillot, M.-L.; Delhaès, P. *Langmuir* **1998**, *14*, 5890. (b) Letard, J.-F.; Nguyen, O.; Soyer, H.; Mingotaud, C.; Delhaès, P.; Kahn, O. *Inorg. Chem.* **1999**, *38*, 3020. (c) Jaiswal, A.; Floquet, S.; Boillot, M.-L.; Delhaès, P. *Chem. Phys. Chem.* **2002**, *12*, 1045.
(8) Seredyuk, M.; Gaspar, A. B.; Ksenofontov, V.; Reiman, S.; Galyametdinov, Y.; Haase, E.; Rentschler, W.; Gütlich., P. *Chem. Mater.* **2006**, *18*, 2513.
(9) Nakamoto, A.; Ono, Y.; Kojima, N.; Matsumura, D.; Yokoyama, T. *Chem. Lett.* **2003**, *32*, 336.
(10) (a) Lètard, J.-F.; Nguyen, O.; Daro, N. *PCT Intl. Appl. WO 2007065996*, 2007. (b) Forestier, T.; Mornet, S.; Daro, N.; Nishihara, T.; Mouri, S.; Tanaka, K.; Fouché, O.; Freysz, E.; Létard, J.-F. *Chem. Commun.* **2008**, DOI: 10.1039/b806347h.
(11) Cobo, S.; Molnar, G.; Real, J. A.; Bousseksou, A. *Angew. Chem., Int. Ed.* **2006**, *45*, 5786.
(12) Boldog, I.; Gaspar, A. B.; Martínez, V.; Pardo-Ibañez, P.; Ksenofontov, V.; Bhattacharjee, A.; Gütlich, P.; Real, J. A. *Angew. Chem., Int. Ed.* **2008**, *47*, 6433.
(13) Molnar, G.; Cobo, S.; Real, J. A.; Carcenac, F.; Daran, E.; Vieu, C.; Bousseksou, A. *Adv. Mater.* **2007**, *19*, 2163.
(14) (a) Volatron, F.; Catala, L.; Riviere, E.; Gloter, A.; Stephan, O.; Mallah, T. *Inorg. Chem.* **2008**, *47*, 6584. (b) Larionova, J.; Salmon, L.; Guari, Y.; Tokarev, A.; Molvinger, K.; Molnar, G.; Bousseksou, A. *Angew. Chem., Int. Ed.* **2008**, DOI: 10.1002/anie.200802906.

Table 1. Crystal Data for 3a

	140 K
empirical formula	$C_{14}H_{10}N_8OPtFe$
*M*r	557.24
cryst syst	tetragonal
space group	*P*4/*mmm*
a (Å)	7.1670(5)
c (Å)	13.0320(13)
V (Å^3)	669.40(9)
Z	1
D_c (mg cm^{-3})	1.382
F(000)	262
μ (Mo Kα) (mm^{-1})	5.773
cryst size (mm^3)	0.08 × 0.10 × 0.10
no. of total reflns	515
No. of reflections [$I > 2\sigma(I)$]	505
R_1 [$I > 2\sigma(I)$][a]	0.0770
wR [$I > 2\sigma(I)$][a]	0.1949
S	1.198

[a] $R_1 = \sum||F_o| - |F_c||/\sum|F_o|$; $wR = [\sum[w(F_o^2 - F_c^2)^2]/\sum[w(F_o^2)^2]]^{1/2}$. $w = 1/[\sigma^2(Fo^2) + (mP)^2 + nP]$ where $P = (F_o^2 + 2F_c^2)/3$; $m = 0.1740$; $n = 0.0000$.

wafers) using the multilayer sequential assembly (MSA) method. The substrates were first functionalized by submersing them overnight into a solution of 30 mM azpy in ethanol. These wafers were soaked for 1 min alternately in 50 mM $Fe(BF_4)_2 \cdot 6H_2O$, 50 mM $\{(TBA)_2[M(CN)_4]\}$ (M = Ni, Pd or Pt), and 50 mM 4,4′-azpy in ethanol solutions, either at −60 °C or at room temperature, in N_2 atmosphere with rinsing in pure ethanol (30 s) after each step. Finally, they were dried under Ar flow. The films were desolvated by a thermal treatment at 160 °C for 30 min. Nanostructured thin films have been obtained in the same way as described in ref. 12 by depositing the multilayers of **1b**−**3b** on a substrate covered by a patterned PMMA film, which was followed by lift-off.

X-ray Crystallography. Diffraction data on crystals of **3a** were collected at 140 K with a Nonius Kappa-CCD single crystal diffractometer using Mo Kα (λ = 0.71073 Å). A multiscan absorption correction was performed but not applied. The absorption correction was found to have no significant effect on the refinement results. The structures were solved by direct methods using SHELXS-97 and refined by full-matrix least-squares on F^2 using SHELXL-97.[15] All non-hydrogen atoms were refined anisotropically. Relevant crystallographic data are displayed in Table 1.

Powder X-ray Diffraction (PXRD). Powder diagrams were collected at room temperature in the range 5° < 2θ < 65° on a Seifert XRD 3003 TT diffractometer, with Bragg−Brentano geometry and Cu tube working at 40 kV with Ni filter (0.3 mm primary slit, 0.3 mm secondary slit, 0.2 mm detector slit and scintillation detector).

Magnetic Susceptibility Measurements. The variable-temperature magnetic susceptibility measurements were carried out between 4 and 400 K using a Quantum Design MPMS2 SQUID magnetometer operating at 1 T magnetic field. The susceptometer was calibrated with $(NH_4)_2Mn(SO_4)_2 \cdot 12H_2O$. The independence of the susceptibility with regard to the applied magnetic field was checked at room temperature for each compound. The temperature was varied at a rate of 1 K min^{-1} in the heating and cooling modes. Experimental susceptibilities were corrected for diamagnetism of the constituent atoms by the use of Pascal's constants.

^{57}Fe Mössbauer Spectroscopy. Mössbauer measurements were carried out in a flow-type liquid nitrogen cryostat using a conventional constant acceleration type Mössbauer spectrometer. γ-Rays were provided by a ^{57}Co(Rh) source (50 mCi). The spectrum evaluations were done with the assumption of Lorentzian line shapes using the Recoil software.[16] All isomer shifts are given relative to α-Fe at room temperature.

Differential Scanning Calorimetry (DSC). Calorimetric measurements have been performed on powder samples of **1a**−**3a** and **1b**−**3b** using a differential scanning calorimeter (Mettler Toledo DSC 821e). Low temperatures were obtained with an aluminum block which was attached to the sample holder, refrigerated with a liquid nitrogen flow, and stabilized at 110 K. The sample holder was kept in a drybox under N_2 flow to avoid water condensation. The measurements were carried out using around 20 mg of a powdered sample sealed in aluminum pans. Temperature and heat flow calibrations were done with standard samples of indium by using its melting transition (429.6 K, 28.45 J g^{-1}). An overall accuracy of 0.2 K in the temperature and 10% in the enthalpy is estimated taking into account the subtraction of the unknown baseline.

Raman Spectroscopy. Variable-temperature Raman spectra were collected in the 150−2300 cm^{-1} frequency range. Samples were enclosed under nitrogen atmosphere on the coldfinger of a THMS600 (Linkam) liquid nitrogen cryostat or under helium atmosphere in a custom-designed Optistat-CF (Oxford Instruments) cryostat (±0.1 K). The LabRAM-HR (Jobin Yvon) Raman spectrometer used in these experiments consists of a confocal optical microscope, a single-grating spectrograph (600 grooves/mm, f = 800 mm) and a DU420-OE (Andor) CCD detector. The entrance slit was kept at 100 μm and a spectral resolution of ca. 2.5 cm^{-1} was obtained. The 632.8 nm line of a 17 mW He−Ne laser was used as the excitation source and plasma lines were removed using a narrow-band interference filter. The exciting radiation was directed through a neutral density filter (OD = 2) to avoid sample heating and was focused on the sample via a 50×, 10.6 mm working-distance objective. The scattered light was collected in a backscattering configuration, using the same microscope objective and the Rayleigh scattering was removed by means of a holographic notch filter. Because of the microcrystalline nature of the samples the polarization of the scattered light was not taken into account.

Microscopic Imaging. Scanning electron microscopy (SEM) images were recorded using a Hitachi S-4800 operating at 1 keV. Atomic force microscopy (AFM) images were collected in ambient conditions in the tapping mode using a Nanoscope Dimension 3100 (Veeco) instrument equipped with an uncoated silicon tip (Nanoworld Arrow NC). The film thickness has been measured at 6 arbitrarily chosen spots for each analyzed sample. A part of the substrate was protected by a PMMA resist during the film deposition and this PMMA mask was removed by rinsing in acetone to provide an uncovered substrate area for the film thickness measurements.

Results

Structure of {Fe(azpy)[M(CN)$_4$]}. As the precedent 3D porous SCO coordination Hofmann polymers {Fe(pyrazine)[M(CN)$_4$]} (M = Ni, Pd, Pt) the present azpy derivatives are highly insoluble and consequently typical samples are constituted of microcrystalline powders. In spite of this, small single crystals of relative good quality were isolated for compound **3a** (M = Pt). Unfortunately, these crystals deteriorated rapidly during the X-ray diffraction experiments at 293 K. This is the reason why we report here only the structural data at 140 K where the system is in the LS state. Like the pyrazine system $\{Fe(azpy)[Pt(CN)_4]\} \cdot H_2O$ crystal-

(15) Sheldrick, G. M. *SHELX97: Program for Crystal Structure Determination*; University of Göttingen: Göttingen, Germany, 1997.

(16) http://www.isapps.ca/recoil/.

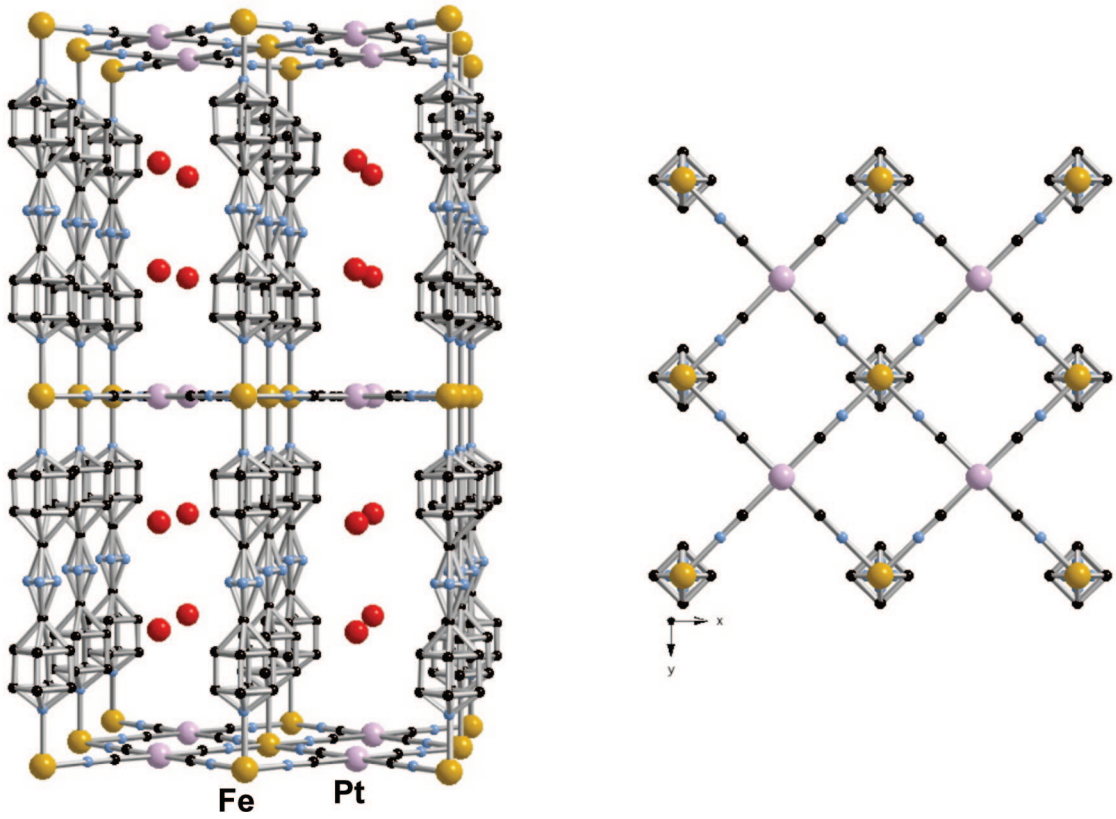

Figure 1. Structure of {Fe(azpy)[(Pt(CN)$_4$)]}· H_2O. View of a fragment of the framework in a direction close to [101] (left) and in the [001] direction (right) (Fe, orange; Pt, pink; O, red; N, blue; C, black).

lize in the tetragonal *P4/mmm* space group (see the Supporting Information). The structure is constituted of an almost regular octahedral site occupied by the iron(II) atom and a square planar site defined by the anion $[Pt(CN)_4]^{2-}$ (Figure 1). The equatorial positions of the $[FeN_6]$ octahedrons are occupied by four nitrogen atoms of different $[Pt(CN)_4]^{2-}$ groups, which act as bridges coordinating to four iron(II) atoms generating parallel $\{Fe[Pt(CN)_4]\}_n$ layers. The layers are pillared by the bismonodentate ligands azpy, which occupy the axial positions of the $[FeN_6]$ octahedrons defining the porous 3D framework. The axial Fe−N(1) distance, 2.01(2) Å, and the equatorial one, 1.9359(2), Å clearly indicate that the compound is essentially in the LS state at 140 K according to its magnetic behavior. Because of severe restrictions imposed by the high symmetry found for the crystal the azpy ligands are strongly disordered and particularly the two nitrogen atoms belonging to the azo group. The Fe····Fe distance through azpy corresponds to the *c* axis of the crystal, 13.0320(13) Å. There is one isolated molecule of water, with occupation factor 0.5, in the unit cell lying in the quaternary axis passing through the two Pt atoms. The distance from these water molecules to the Pt atoms is 4.56(2) Å, whereas the distance between the water molecules is 3.91(2) Å. For this monohydrate form, the solvent accessible void space was estimated to be 121 Å^3. The center of gravity of this void is located between the azpy pillars just in the plane (001) defined by the disordered azo groups. The total accessible solvent void space without the water molecules is 286 Å^3 (43%).

Figure 2 compares the XRPD pattern calculated from the single crystal data with the experimental pattern of a

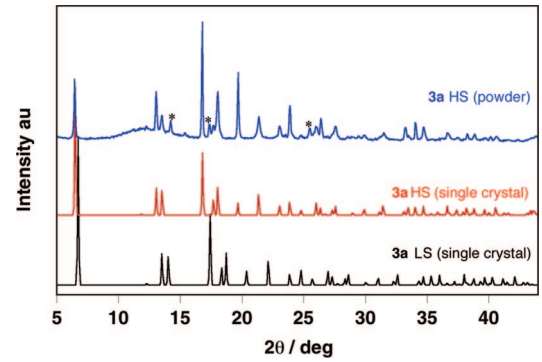

Figure 2. X-ray powder diffraction patterns of **3a**: calculated from single-crystal data at 140 K in the low-spin state (black), calculated for the high-spin state (red) and experimental (blue).

sample constituted of grinded crystals of **3a**. It is important to note that although both spectra are clearly related, there are notable differences between them. On one hand, there is a systematic shift of the reflections toward lower 2θ values, which is related to the different spin state of each sample. The calculated spectrum corresponds to the crystal in the LS state, whereas the experimental pattern was registered at 300 K where the compound is mostly HS (>98% HS). Taking into account the high symmetry of the crystal, it is easy simulate an XRPD spectrum of **3a** in the HS state with $a = b = 7.440$ Å and $c = 13.550$ Å. These values are consistent with a hypothetical increase Δ[Fe−N(1)] = 0.259 Å and Δ[Fe−N(2)] = 0.193 Å upon LS-to-HS spin state conversion and correspond to an expected average Δ[Fe−N] variation of 0.215 Å. As can be seen in Figure 2, **3a** Pt(HS), there is a satisfactory correspondence between this spectrum

and the experimental spectrum Pt(HS). Indeed, most of peaks of the experimental spectrum can be tentatively indexed. The most significant one corresponds to the reflection plane (001) at $2\theta = 6.52°$ ($d \approx 13.550$ Å) defined by the $\{Fe[Pt(CN)_4]\}_n$ layers separated by the azpy ligands which coordinates two iron atoms of consecutive layers. Despite the reasonably good match between both spectra there are four significant reflections in the experimental spectrum that do not correspond to the calculated one (noted with the symbol *). A plausible hypothesis is that grinding the single crystals generates distortions and other defects in the unit cell. The diffractograms of the precipitated samples of the Pt derivative are practically identical to that of the grinded crystals. The precipitated samples of the Pd derivative also match quite well that of the Pt, the (001) reflection appears at $2\theta = 6.54°$ ($d \approx 13.503$ Å). However, although the spectrum of the Ni derivative is also quite similar it clearly denotes some differences that could be assigned to its smaller ionic radius and the occurrence of distortions in the framework ($2\theta = 6.68°$, $d(001) \approx 13.223$ Å) (see the Supporting Information). In summary, from these data it is safe to conclude that **1a**−**3a** display quite similar crystal structures in both spin states.

Magnetic Properties. Figure 3 shows the thermal dependence of the $\chi_M T$ product (where χ_M stands for the molar magnetic susceptibility) of the hydrated and dehydrated powders of the compounds $\{Fe(azpy)[M(CN)_4]\}\cdot nH_2O$ (M = Ni, Pd or Pt; $n = 1, 0$). At 300 K, the $\chi_M T$ product has a value of 2.9 $cm^3\ mol^{-1}$ K (**1a**, **1b**) and 3.2 $cm^3\ mol^{-1}$ K (**2a**, **2b**, **3a**, **3b**) indicating that most of the iron(II) ions are in the HS state (S = 2) at this temperature. In the case of the hydrated and dehydrated Ni analogues (**1a**, **1b**), similar behaviors have been observed, $\chi_M T$ diminishes slightly from 300 K down to 250 K, 2.72 $cm^3\ mol^{-1}$ K, and then more abruptly reaching a value of 0.8 $cm^3\ K\ mol^{-1}$ at 200 K. A subsequent slight decrease is observed between 200 and 100 K, where $\chi_M T$ is 0.7 $cm^3\ K\ mol^{-1}$, indicating that the Fe(II) ions undergo an incomplete and moderately cooperative spin transition with $T_c = 245$ K. No hysteresis is observed upon heating. The decrease of $\chi_M T$ below 50 K occurs because of the zero-field splitting of the Fe(II) ions remaining in the HS configuration and/or due to antiferromagnetic interactions. On the contrary, the Pd (**2a**) and Pt (**3a**) analogues display first order phase transitions with hysteresis loops located at $T_c{\downarrow} = 287$ K (**2a**), 275 K (**3a**) and $T_c{\uparrow} = 296$ K (**2a**), 285 K (**3a**). However, the transitions are not complete and the $\chi_M T$ value at 100 K is ca. 0.8 for both compounds. These values are slightly higher than what can be expected for the pure LS phase, indicating therefore that a small HS residual fraction remains in each compound even at very low temperatures. The dehydrated derivatives **2b** and **3b** also undergo steep spin transitions. However, the magnetic behavior of the hydrated and dehydrated compounds is significantly different: for **2b** and **3b**, the transition is shifted to lower temperatures by ca. 100 K ($T_c{\downarrow} = 181$ K (**2b**), 175 K (**3b**) and $T_c{\uparrow} = 202$ K (**2b**), 190 K (**3b**)) and the hysteresis is by 10 K larger in comparison with **2a** and **3a**. It is a clear evidence of the effect of the water molecules on the spin transition phenomena in these compounds.

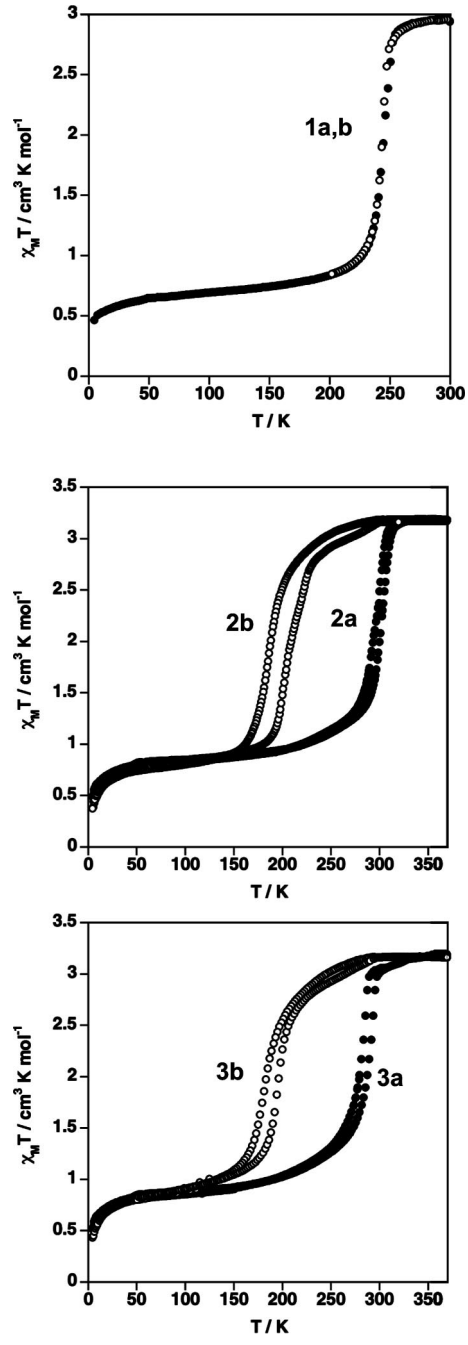

Figure 3. Magnetic properties, in the form of $\chi_M T$ vs T curves, of $\{Fe(azpy)[(M(CN)_4)]\}\cdot nH_2O$ (M = Ni, Pd or Pt) powders upon heating and cooling. Ni, **1a** ($n = 1$), **1b** ($n = 0$); Pd, **2a** ($n = 1$), **2b** ($n = 0$); and Pt, **3a** ($n = 1$), **3b** ($n = 0$).

Mössbauer Spectroscopy. Mössbauer spectra of the hydrated and dehydrated samples are displayed in Figure 4 and the corresponding spectrum parameters and errors are listed in Table 2. For each compound, the hyperfine parameters of the main quadrupolar doublets at 80 K and around 300 K correspond well to the typical parameters of ferrous LS and HS complexes, respectively, confirming thus the occurrence of SCO in each sample. It is interesting to note the relatively low quadrupole splitting values in the HS state compared to typical values of SCO compounds with $Fe^{II}N_6$ coordination core. This observation may be related to the unusually high symmetry of the complex. In agreement with the magnetic measurements, small amounts of residual

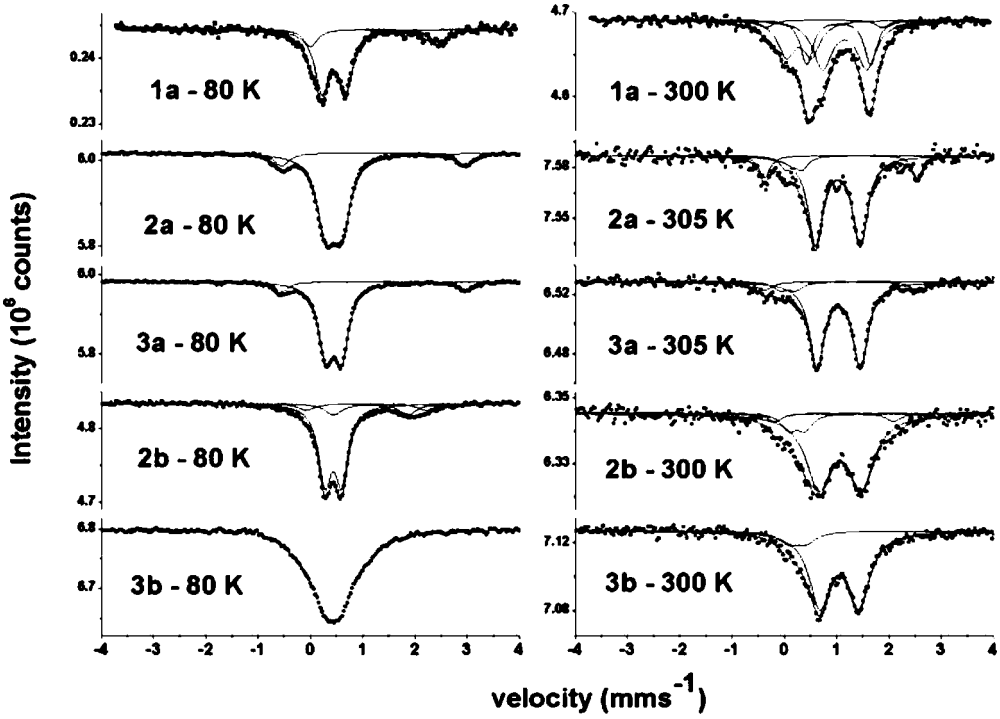

Figure 4. Mössbauer spectra of **1a**−**3a** and **2b**−**3b** (powder samples) recorded at various temperatures.

Table 2. Hyperfine ^{57}Fe Mössbauer Parameters and Their Statistical Errors (in parentheses) for 1a−3a and 2b−3b at High and Low Temperatures[a]

		T (K)								
		1a		2a		3a		2b		3b[b]
		80	280	80	305	80	305	80	300	300
LS	δ	0.446(7)	0.28(6)	0.444(2)	0.18(6)	0.446(2)	0.08(8)	0.437(3)	0.24(8)	0.24(8)
	Δ	0.44(1)	0.48(1)	0.303(4)	0.30	0.299(3)	0.30	0.320(5)	0.30	0.3(1)
	$\Gamma/2$	0.161(9)	0.2	0.191(3)	0.14	0.162(3)	0.17	0.148(4)	0.17	0.2(1)
	A/A_{tot}	77	27	85	9	88	8	75	10	13
HS1	δ		1.16(2)		1.024(8)		1.038(6)	1.15(2)	1.06(2)	1.05(1)
	Δ		0.85(9)		0.86(2)		0.83(1)	1.42(4)	0.82(4)	0.74(2)
	$\Gamma/2$		0.22(3)		0.17(1)		0.173(8)	0.20	0.29(3)	0.25(1)
	A/A_{tot}	0	42	0	76	0	83	15	84	87
HS2	δ	1.23(2)	1.04(2)	1.20(1)	1.08(2)	1.22(1)	1.08(5)	1.07(3)	0.95(9)	
	Δ	2.45(4)	1.22(3)	3.51(2)	2.93(5)	3.51(2)	2.9(1)	2.29(8)	2.3(2)	
	$\Gamma/2$	0.16	0.14(3)	0.18(2)	0.12(4)	0.17(2)	0.17	0.20	0.17	
	A/A_{tot}	23	25	15	14	12	9	10	6	0

[a] A/A_{tot} (%), δ (mms^{-1}), Δ (mm s^{-1}), and $\Gamma/2$ (mm s^{-1}) signify the relative amount of the subspectra, the isomer shift, the quadrupole splitting, and the half-width at half height, respectively. Values without parentheses were fixed during the fitting. [b] No reliable fitting could be performed of **3b** at 80 K with the assumption of Lorentzian line shapes.

HS and LS iron species (i.e., SCO inactive) have been observed in each Mössbauer spectra at low and high temperature, respectively. The residual HS species exhibit distinct hyperfine parameters with respect to the SCO active HS species. This species may be assigned to lattice defects or to impurities. Interestingly, the spectra of the dehydrated compounds **2b** and **3b** display line broadenings typical of rapid interconversion of spin states.[17] This indicates that the dehydratation and, presumably, host−guest interactions in general have a strong influence on the dynamics of intersystem crossing of the iron(II) ions in these porous systems. Such a finding would not be entirely unexpected taking into account the sensibility of the SCO phenomenon to modifications of the crystal lattice.

DSC Analysis. The calorimetric data were recorded in the heating and cooling modes in order to evaluate the enthalpy (ΔH) and entropy (ΔS) variations associated with the spin transitions of **1a**−**3a** and **1b**−**3b** (Figure 5). The DSC curve show a singularity at $T_c = 245$ K **1a**. The Pd samples, in the hydrated and dehydrated forms, show one maximum in the cooling mode and two in the heating mode [$T_c\downarrow = 282$ K, $T_{c1}\uparrow = 296$ K, $T_{c2}\uparrow = 310$ K for **2a** and $T_c\downarrow = 186$ K, $T_{c1}\uparrow = 204$ K, $T_{c2}\uparrow = 226$ K for **2b**]. In the case of Pt, the DSC curves show two maxima for **3a** in the cooling and heating modes [$T_{c1}\downarrow = 301$ K, $T_{c2}\downarrow = 293$ K, $T_{c1}\uparrow = 301$ K, $T_{c2}\uparrow = 307$ K] and one for the **3b** complexes [$T_c\downarrow = 166$ K, $T_c\uparrow = 309$ K]. These values agree reasonably well with those obtained from the magnetic measurements. The two-step features observed in the calorimetric measurements might

(17) Thiel, A.; Bousseksou, A.; Verelst, M.; Varret, F.; Tuchagues, J. P. *Chem. Phys. Lett.* **1999**, *302*, 549.
(18) (a) Bell, C. M.; Arendt, M. F.; Gomez, L.; Schmeh, R. H.; Mallouk, T. E. *J. Am. Chem. Soc.* **1994**, *116*, 8314. (b) Bell, C. M.; Keller, S. W.; Lynch, V. M.; Mallouk, T. E. *Mater. Chem. Phys.* **1993**, *35*, 225.

be an indication of subtle structural modifications taking place concomitantly with the SCO for **2a**, **2b** and **3a**. The estimated ΔH and ΔS variations for the spin transition are 5.9 kJ mol^{-1} and 24 J K^{-1} mol^{-1} (**1a**), 15.6 kJ mol^{-1} and 50 J K^{-1} mol^{-1} (**2a**) 7.8 kJ mol^{-1}, and 42 J K^{-1} mol^{-1} (**2b**) and 15.7 kJ mol^{-1} and 52 J K^{-1} mol^{-1} (**3a**) 7.7 kJmol^{-1}, and 37 J K^{-1} mol^{-1} (**3b**), respectively. These values are common for iron(II) spin crossover compounds. As expected, the ΔS values are significantly larger than the entropy variation resulting from the sole change in spin multiplicity ($\Delta S = R \ln[(2S_{HS} + 1)/(2S_{LS} + 1)] = 13.4$ J mol^{-1} K^{-1} for $S_{HS} = 2$ and $S_{LS} = 0$). The excess of entropy mainly corresponds to the structural changes associated with the $[FeN_6]$ coordination core. The longer Fe−N bond lengths in the HS state lead to the decrease of the interatomic force constants thereby reducing the vibrational frequencies. As a result, the density of vibrational states increases in the low frequency range and, consequently, the vibrational entropy increases upon the LS to HS transition.[1]

Film Growth. Thin films of the compounds {Fe(azpy)[$M(CN)_4$]} (M = Ni, Pd or Pt) (**1b**−**3b**) were assembled using the multilayer sequential assembly technique (MSA) (Figure 6) in a similar way as described in refs 11 and 18. The thin layers were successfully deposited on clean gold substrates, either at −60 °C or at room temperature. It is interesting to note here that thin films of {Fe(pyrazine)[$M(CN)_4$]} could be grown only at low temperature.[11] The formation of the {Fe(azpy)[$M(CN)_4$]} films is indicated by a change of coloration of the substrate. The coloration of the films becomes deeper with increasing number of dipping cycles. To follow the growth of the films AFM measurements were performed (Figure 8). Figure 7 shows a plot of film thickness as a function of the number of deposition cycles for {Fe(azpy)[$Pd(CN)_4$]} (**2b**), derived from AFM measurements. As expected, the film thickness increases monotonously with the number of dipping cycles and the measurements reveal a thickness of ca. 10 nm for the film after 4 deposition cycles, and ca. 22 nm for 10 deposition cycles. Considering that the ligand azpy separates ca. 1.35 nm two consecutive metal atoms, the expected film thickness for 4 and 10 cycles is ca. 5.4 and 13.5 nm, respectively. These values are significantly higher than what could be expected for the assembly of a single {Fe(azpy)[$Pd(CN)_4$]} layer in each deposition.

Micro- and nanometric patterns of the films were also successfully obtained, similar to the case of {Fe(pyrazine)[$M(CN)_4$]},[13] using a PMMA mask as a physical barrier for the assembly of the multilayers on the substrate. Figure 9 displays the SEM images of various square and rodlike patterns with different sizes between 2 μm and 30 nm. We can see that dense arrays of submicronic features with periods down to 200 nm were successfully lifted.

Raman Spectroscopy. To control the composition and structure of the thin films as well as to probe their spin state, we have carried out comparative Raman spectroscopy measurements taking the anhydrous bulk materials **1b**−**3b** as references. To get good signal-to-noise response, we adjusted the thickness of the films to ca. 100 nm. It is worth noting that the thin films and powders can only be compared

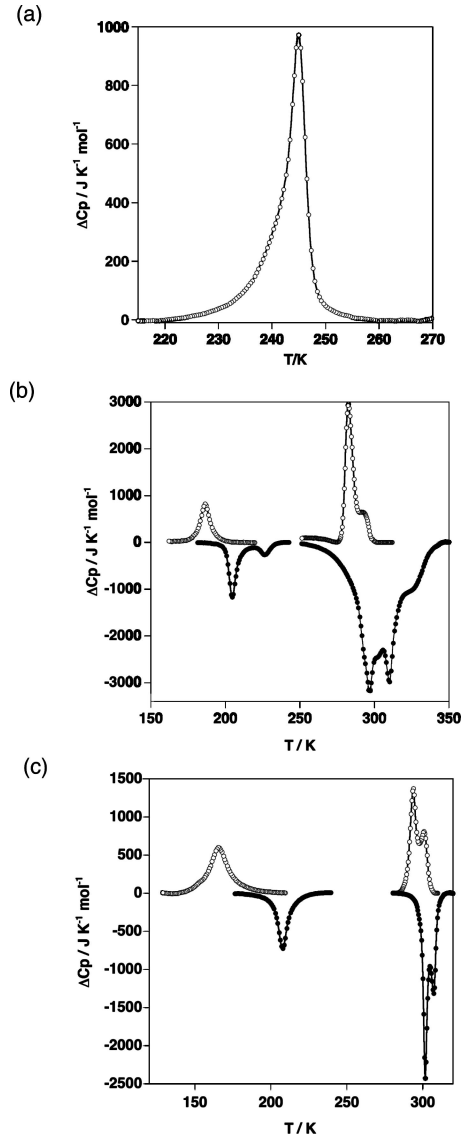

Figure 5. DSC analysis for **1a**−**3a** and **2b**−**3b** (powder samples).

in the desolved forms (**1b**−**3b**). The assignment of CN stretch and ligand modes was carried out on the basis of literature data[19,20] and using DFT calculations on the azpy molecule (see the Supporting Information). The CN stretch, as expected, appears around 2200 cm^{-1} in the Raman spectra. Compared to the corresponding $K_2M(CN)_4$ compounds, the ν (CN) modes are shifted to higher frequencies by 40−50 cm^{-1}, which is a general trend when going from the terminal (M−CN) to the bridging (M−CN−M′) cyanide ligands. In the region between 1600 and 600 cm^{-1}, several bands have been assigned to the azpy ligand by comparing to the spectrum of the pure azpy. The vibrational modes in the 1600−990 and 730−660 cm^{-1} ranges can be attributed to the azopyridine ring stretching and bending or twisting modes, respectively. The spectral features below 600 cm^{-1} can be assigned mainly to normal modes corresponding to metal−ligand vibrations, but their proper assignment is

(19) Molnár, G.; Niel, V.; Gaspar, A. B.; Real, J. A.; Zwick, A.; Bousseksou, A.; Mc-Garvey, J. J. *J. Phys. Chem. B* **2002**, *106*, 9702.
(20) Zhuang, Z.; Cheng, J.; Wang, X.; Yin, Y.; Chen, G.; Zhao, B.; Zhang, H.; Zhang, G. *J. Mol. Struct.* **2006**, *794*, 77.

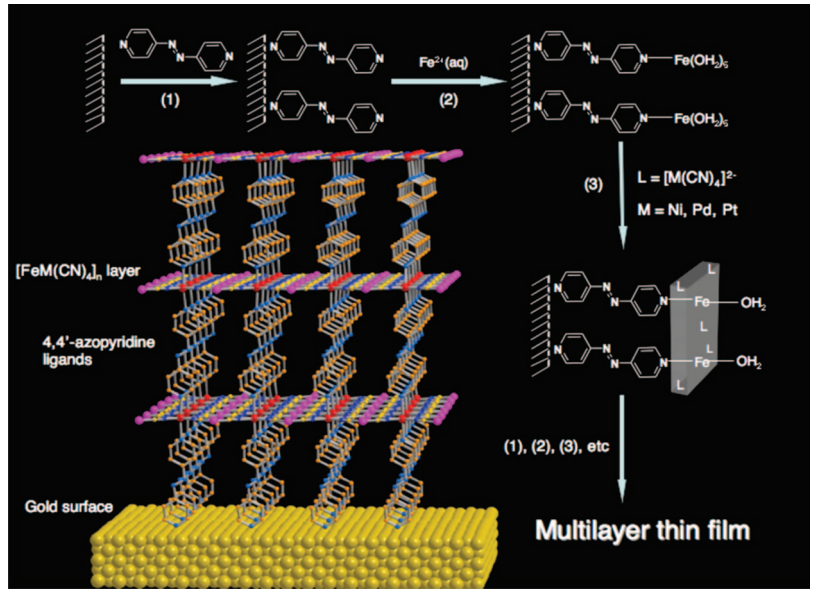

Figure 6. Schematic representation of the sequential assembly of {Fe(azpy)[(M(CN)$_4$)]} (M = Ni, Pd, or Pt) (**1b**−**3b**) thin films.

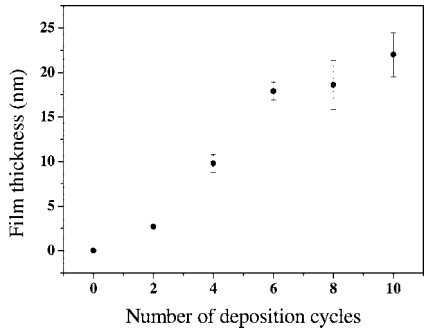

Figure 7. Evolution of the mean thickness of {Fe(azpy)[Pd(CN)$_4$]} (**2b**) multilayers as a function of the dipping cycles. (The film thickness has been measured by AFM.)

difficult because of the low signal intensity and the strong coupling between the different modes.[19]

Figure 10 displays the Raman spectra of the dehydrated compound **2b** in the powder and thin film forms recorded between 600 and 1700 cm^{-1} at 300, 150, and 5 K. Spectra of **1b** and **3b** display fairly similar features in this spectral range as shown in the Supporting Information. According to the magnetic data, at 300 and 150 K the powder samples are in the HS and LS states, respectively. Indeed, we observed a clear difference between the two spectra, especially in the region of internal Raman modes of the azpy ligand between 1000 and 1600 cm^{-1}, which are strongly enhanced in intensity when going from the HS to the LS state. Furthermore, the HS modes around 1014 and 1467 cm^{-1} (assigned to ring breathing and ring stretching modes, respectively), exhibit in the LS state a frequency shift to 1027 and 1450 cm^{-1}, respectively. However, a very good marker of the spin state change is the Raman mode around 1497 cm^{-1}. On the other hand, an interesting observation has been made in the spectra recorded at 5 K, indicating the reappearition of the HS state at this temperature both in the powder sample and the thin film. Indeed, it is well-known that a light-induced LS-to-HS conversion can be achieved in many Fe(II) SCO compounds at temperatures well below the thermal transition temperature, where the HS to LS relaxation rate becomes sufficiently slow.[1b] We can thus straightforwardly attribute this observation to the so-called light-induced excited spin state trapping (LIESST) effect, induced by the laser light (633 nm), which is used to excite the Raman scattering.[21] Similar photoinduced phenomena appear also in the case of the Pt and Ni complexes with the exception of the powder form of the Ni complex (see the Supporting Information).

If the relative integrated intensity of the 1497 cm^{-1} mode and that at 1415 cm^{-1} is plotted as a function of the temperature for powder samples, the obtained curve resembles to the $\chi_M T$ vs T curve (Figure 11). A significantly better match between the thermal spin transition curves obtained from magnetic and Raman measurements cannot really be expected because the intensity of the Raman signal is not strictly proportional to the spin fractions and because of eventual laser-light-induced effects (heating, etc.). Nevertheless, according to the Raman data displayed in Figure 11, it is obvious that the SCO behavior (thermal and light-induced) is very similar for powder and thin film samples containing the same metal (Ni, Pd, or Pt). Apart from small temperature shifts, the only significant difference between the thin film and powder samples appears in the Ni case, where the bulk sample exhibits only a weak light-induced spin state change. This difference might be related to the fact that the color of the Ni sample (dark green) differs from the other two samples (dark violet).

Discussion

This work was undertaken aiming at exploring the spin crossover phenomenon of novel porous Hofmann metalorganic frameworks exhibiting larger porosity than the previous

(21) (a) Suemura, N.; Ohama, M.; Kaizaki, S. *Chem. Commun.* **2001**, 1538. (b) Ould Moussa, N.; Molnár, G.; Ducros, X.; Zwick, A.; Tayagaki, T.; Tanaka, K.; Bousseksou, A. *Chem. Phys. Lett.* **2005**, *402*, 503. (c) Ould Moussa, N.; Molnár, G.; Bonhommeau, S.; Zwick, A.; Mouri, S.; Tanaka, K.; Real, J. A.; Bousseksou, A. *Phys. Rev. Lett.* **2005**, *94*, 107205.

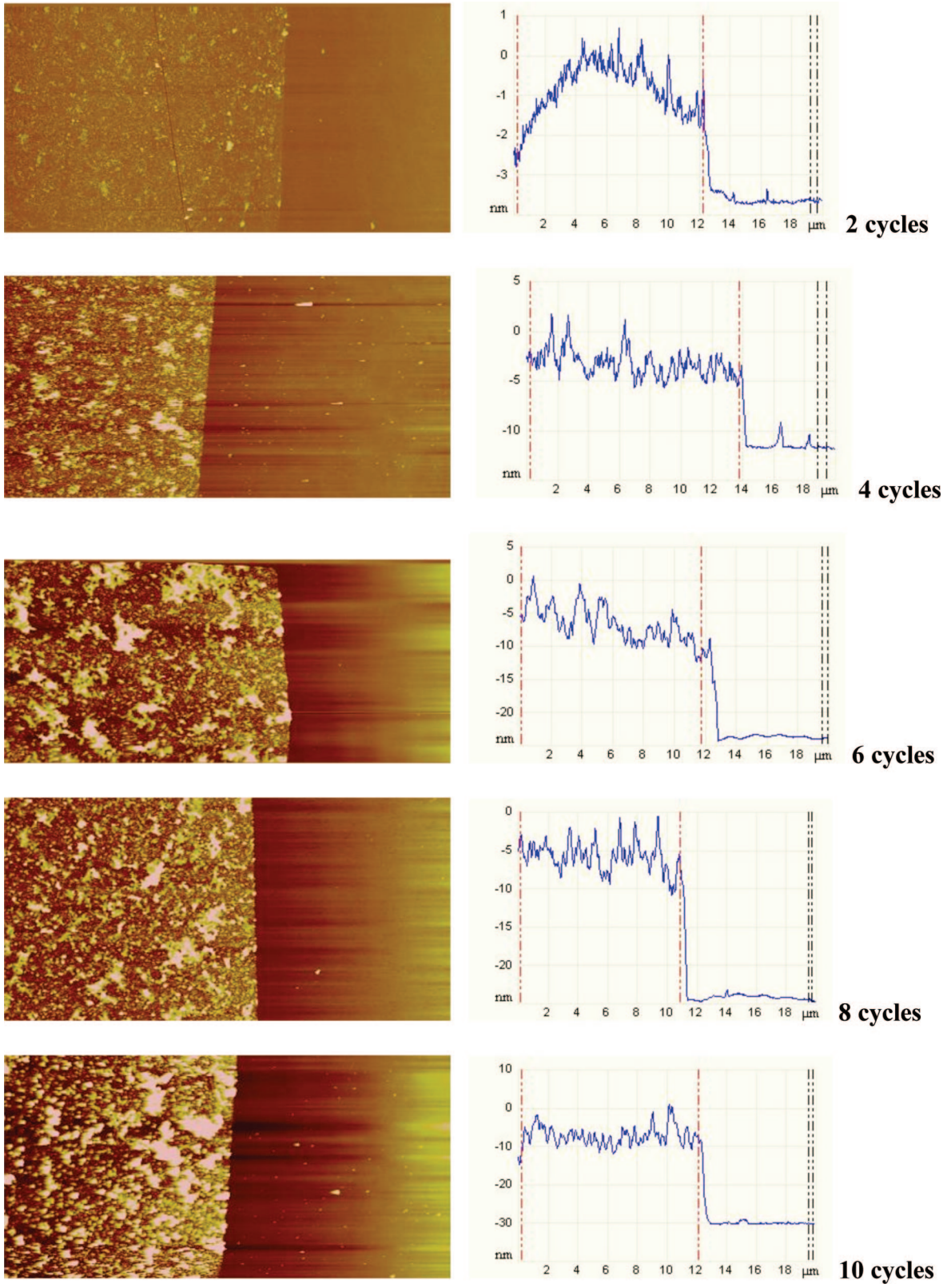

Figure 8. Representative AFM images and cross-sections of thin films of **2b** following 2, 4, 6, 8, or 10 deposition cycles. (Image size, 20 × 10 μm^2; color scale (height), 0−50 nm.)

ones derived from the bis-monodentate bridging pyrazine ligand. Our first choice was to replace the pyrazine pillar by the ligand azpy. X-ray diffraction analyses of the resulting new solids clearly indicate that they display basically the same tetragonal *P4/mmm* space group, as the pyrazine derivatives do. The major difference is ascribed to the size of the bridging ligands. Pyrazine separates consecutive $\{Fe[M(CN)_4]\}_n$ layers by ca. 7.3 Å, whereas in azpy, they are separated by ca. 13.5 Å, thereby increasing the solvent accessible voids from ca. 131 to 286 $Å^3$. As far as we know, this is the largest accessible volume found for a Hofmann clathrate reported up to now. For example the separation

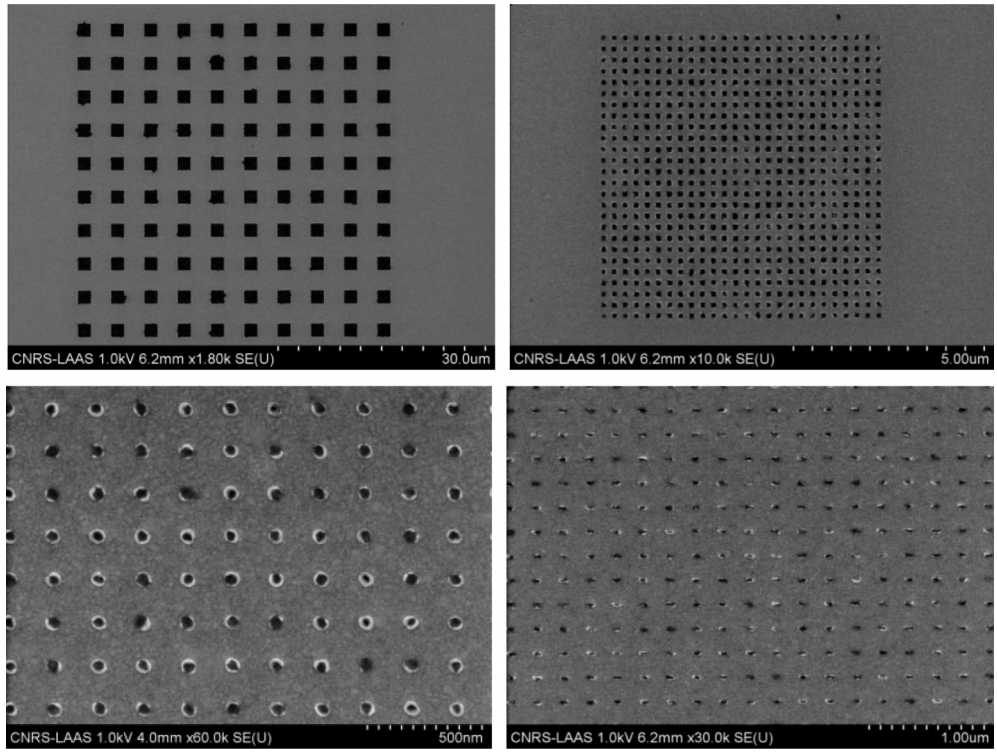

Figure 9. SEM images of patterns of {Fe(azpy)[Pd(CN)$_4$]} (**2b**) obtained following 10 deposition cycles. Lateral pattern sizes: (a) 2 × 2 μm, (b) 200 × 200 nm, (c) 50 × 50 nm, (d) 80 × 30 nm.

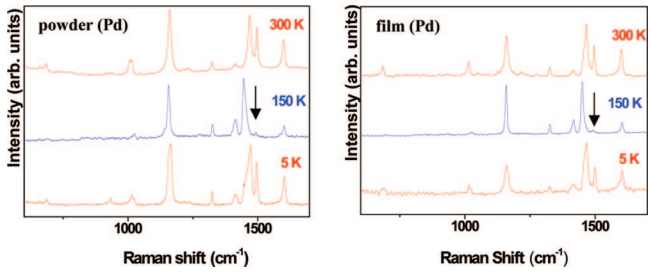

Figure 10. Raman spectra of {Fe(azpy)[Pd(CN)$_4$]} (**2b**) powders and thin films recorded at 300, 150, and 5 K.

between the layers of the 2D polymer {Fe(NH$_3$)$_2$[Ni(CN)$_4$]}·(thiophene) is 7.941 Å[22] or for the 3D frameworks {Cd(L-L)$_2$[Ni(CN)$_4$]}·(pyrrole) where L-L is ethylenediamine and 1,4-butanediamine is 7.861[23] and 7.840 Å,[24] respectively. In spite of the large difference of accessible solvent volume between pyrazine and azpy derivatives, the latter precipitate systematically as monohydrate species unlike the pyrazine derivatives in which the dihydrate is the most stable form, although higher hydrates can also be isolated.

Similarly to the pyrazine compounds, the spin crossover behavior starts near 300 K for **1a**−**3a**. However, a major difference corresponds to the cooperativity of the spin transition, which is markedly smaller for **1a**−**3a** compounds, a fact that might be associated with the less-rigid nature of the azpy ligand.

Another important singularity is the strong dependence of the spin crossover on the water molecules loaded in the lattice. This is an important aspect, which transcends the fact of whether the SCO solid is porous or not. Influence of solvent molecules on the SCO behavior has been recognized since the very first studies of this phenomenon. Solvents can directly influence the electronic

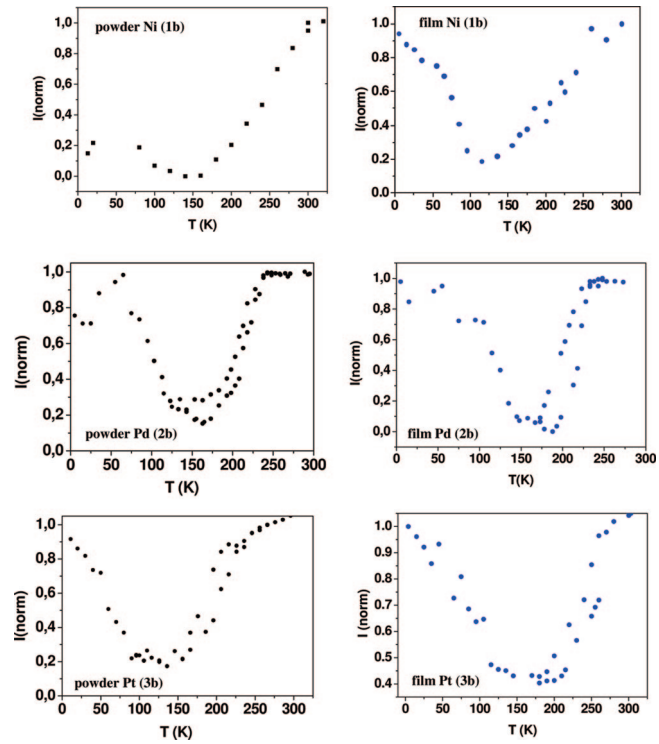

Figure 11. Temperature dependence of the Raman intensity ratio (I(1497 cm^{-1})/I(1415 cm^{-1})) for {Fe(azpy)[M(CN)$_4$]} (M = Ni, Pd or Pt) **1b**−**3b** powder and film samples upon cooling and heating. (The curves have been scaled using the magnetic susceptibility data of the powder samples.)

(22) Kitazawa, T.; Gomi, Y.; Takahashi, M.; Takeda, M. *Mol. Cryst. Liq. Cryst.* **1998**, *311*, 167.
(23) Iwamoto, T.; Kiyoki, M. *Bull. Chem. Soc. Jpn.* **1975**, *48*, 2412.
(24) Nishikiori, S. I.; Iwamoto, T. *Inorg. Chem.* **1986**, *25*, 788.

configuration of the SCO center via formation of hydrogen bonds (i.e., hydroxylic solvents)[25] and/or indirectly influencing on the crystal packing, which modulates the geometry of the $[FeN_6]$ core thereby determining the SCO properties.[26] Obviously, the latter effect is important for 0D SCO complexes whereas for polymeric SCO compounds it should be minimized as the polymerization degree increases from 1D to 3D. In this respect, although the number of well characterized 2−3D polymeric SCO compounds is still limited, it is safe to state that the dependence of the SCO properties on solvation, in these systems, is dictated by local interactions (hydrogen bonds) between the hydroxylic solvent and some ligand atoms placed close to the $[FeN_6]$ core, rather than overall framework geometry changes.[27,28] Anyway, both types of electronic effects fine-tune the ligand field strength at the iron centers and are well-known in the spin crossover field. However, it cannot be excluded other kinds of host−guest interactions with chemically distinct solvents. Interplay between host−guest chemistry and spin crossover phenomena is being currently studied in detail in these frameworks, but this is not in the scope of the present paper.

The crystal structure of **3a** clearly shows that there are two water molecules occupying equivalent positions just located in the imaginary vertical line connecting the two Pt atoms of the unit cell. They do not interact either to each other or with the walls of the cavity. The smaller size of the pyrazine ligand only allows the placement of one water molecule between the two Pt atoms in $\{Fe(pyrazine)[Pt(CN)_4]\}\cdot 2H_2O$, the Pt···O distance is 3.607(3) Å. The other molecule of water is placed between the pyrazine ligands showing short C···O contacts (2.576(2) Å), indicating strong interaction with the pillars.[3] It is worth noting that the latter interactions do not occur in the azpy derivative because the equivalent site is empty. Dehydration destabilizes the LS state decreasing $T_{1/2}$ ca. 100 K in **2b** and **3b**, whereas much smaller differences between the dihydrate and unsolvate forms are found for the pyrazine compounds.[5] These observations could be related, in principle, to the more flexible nature of the azpy ligand, which can afford subtle distortions in the framework, whereas the more rigid pyrazine network is apparently less affected by the solvent molecules. The fact that **1a** displays only small SCO differences compared to **1b** needs further investigations.

The photoinduced transformation of the LS state into the HS state at temperatures below ca. 130 K upon red light irradiation, the LIESST effect, is another singularity that differentiates **1b**−**3b** from $\{Fe(pyrazine)[M(CN)_4]\}$. It should be noted, however, that the transition temperatures and thus the zero-point energy diferences (ΔE_0) are much lower in **1b**−**3b** when compared to $\{Fe(pyrazine)[M(CN)_4]\}$. Because the activation energy of the HS→LS relaxation increases with decreasing ΔE_0, it is thus not surprising that the stability of the photoinduced metastable HS state is higher in the azpy derivatives.[1b] On the other hand, one may expect similar nanosecond-laser-shot-induced effects in the azpy derivatives as were observed in the pyrazine compounds within the thermal hysteresis region,[6] even if the investigation of such phenomena will be more challenging in the former family because of the narrower and less rectangular hysteresis loops.

The availability of these polymers to be processed as micro- and nanopatterned thin films preserving their SCO properties has also been a primary goal of this work. To do so, we have followed the synthetic method used for processing $\{Fe(pyrazine)[M(CN)_4]\}$ thin films, which is a variant of the so-called "sequential ligand exchange reaction" described by Mallouk and co-workers. It takes advantage of the fact that the ligand azpy forms a fairly continuous monolayer and adopts a perpendicular orientation on silver surfaces with respect to the plane of the molecule.[20] In fact, we realized that this self-assembled monolayer is also stable on gold surfaces and facilitated the build up of films of $\{Fe(pyrazine)[M(CN)_4]\}$. Thus, in a first step, azpy anchors the gold surface (Figure 6, (1)), and then steps (2) and (3) (Figure 6) generate the first $\{Fe[M(CN)_4]\}_n$ layer. Finally, the cycle (1)−(3) is repeated several times, generating the architecture of the 3D porous Hofmann-like SCO frameworks **1b**−**3b**. It is clear that the experimental conditions we used facilitate a more complex growth mechanism than the idealized layer-by-layer picture (Figure 6). Most probably, a real picture of the thin film would not correspond to a true epitaxial growth, but a multinucleation process and 3D-like growth ending in a polycrystalline film. Whatever the texture of the thin film, the SCO property is retained.

Conclusion

A family of novel porous coordination polymers of the Hofmann type displaying thermal and light-induced spin crossover phenomena has been synthesized as bulk microcrystalline powders. The structural analyses demonstrate that these materials show an improved pore size with respect precedent examples of Hofmann clathrates. These new open-framework functional structures have also been covalently bound to a gold surface giving either continuous or micro- and nanopatterned thin films. The intrinsic switchable nature of these materials together with their porosity and availability to be processed at small scales make them excellent platforms for a new generation of sensory and memory materials based on interplay and/or synergy stemming from coexistence of spin crossover and host−guest chemistry.

Acknowledgment. This work was supported by the RTB program of the LAAS-CNRS (Toulouse, France), the Spanish Ministerio de Educacion y Ciencia (MEC) (CTQ2007-64727/BQU), and the Acción Integrada Hispano-Francesa del MEC HF2005-0117. The authors acknowledge financial support from the Agence National de la Recherche (NANOMOL project), the European Action COST D35, and the French Embassy in

(25) Gütlich, P. *Struct. Bonding* **1981**, *44*, 83.
(26) Real, J. A.; Muñoz, M. C.; Andrés, E.; Granier, T.; Gallois, B. *Inorg. Chem.* **1994**, *33*, 3587.
(27) Vreugdenhil, W.; van Diemen, J. H.; De Graaff, R. A. G.; Haasnoot, J. G.; Reedijk, J.; Kahn, O.; Zarembowitch, J. *Polyhedron* **1990**, *9*, 2971.
(28) Halder, G. J.; Kepert, C. J.; Moubaraki, B.; Murray, K. S.; Cashion, J. D. *Science* **2002**, *298*, 17627.

Hungary. A.B.G. thanks the Spanish MEC for a research contract (Programa Ramón y Cajal). We are grateful to L. Rechignat (LCC) and F. Carcenac (LAAS) for technical help in Raman spectroscopy and e-beam lithography.

Supporting Information Available: Thermogravimetric analysis, X-ray diffraction patterns, and differential scanning calorimetric data of powder samples; Raman spectra of powder and thin film samples; experimental and calculated Raman active vibrational frequencies of $\{Fe(azpy)[(M(CN)_4)]\}\cdot nH_2O$ (M = Ni, Pd or Pt) and the 4,4′-azopyridine molecule; CIF file of compound **3a** (PDF). This material is available free of charge via the Internet at http://pubs.acs.org.

CM8019878